Density functional theory investigation of the electronic and optical properties of metallo-phthalocyanine derivatives

Zouaghi, Mohamed Oussama; Arfaoui, Youssef; Champagne, Benoît

Published in:
Optical Materials

DOI:
10.1016/j.optmat.2021.111315

Publication date:
2021

Document Version
Publisher's PDF, also known as Version of record

Optical Materials 120 (2021) 111315

Contents lists available at ScienceDirect

Optical Materials

journal homepage: www.elsevier.com/locate/optmat

Research Article

Density functional theory investigation of the electronic and optical properties of metallo-phthalocyanine derivatives

Mohamed Oussama Zouaghi [a,b], Youssef Arfaoui [a], Benoît Champagne [b,*]

[a] Department of Chemistry, Laboratory of Characterizations, Applications and Modeling of Materials LR18ES08, University of Tunis El Manar, Tunisia
[b] Laboratory of Theoretical Chemistry, Unit of Theoretical and Structural Physical Chemistry, Namur Institute of Structured Matter, University of Namur, Rue de Bruxelles, 61, 5000, Namur, Belgium

ARTICLE INFO

Keywords:
Metallo-phthalocyanines
DSSCs
Electronic and optical properties
Density functional theory

ABSTRACT

The electronic and optical properties of metallo-phthalocyanine derivatives have been calculated by using density functional theory. Starting from a reference Zn(II) phthalocyanine the structure has been varied by changing the nature of the transition metal, by adding carboxylic functions, as well as by considering the extension of the aromatic rings with fused phenyl moieties, with the perspective of optimizing their performance as sensitizers in solar cells. Calculations demonstrate that the transition metal (Ni, Mn, Fe, Co, and Cu *versus* Zn) has a small impact on the free energies of the primary processes (injection, recombination, and regeneration), that adding several carboxylic acid functions has a cooperative role to optimize the injection process, and that the addition of fused phenyl rings increases the light harvesting efficiency and the free energy of injection.

1. Introduction

Dye-sensitized solar cells (DSSCs) have attracted significant attention as low-cost alternatives to conventional solid-state photovoltaic devices [1–6]. Many investigations have aimed at enhancing the efficiency of each process involved in DSSCs [7–10]. In DSSCs, the dye acts as a sensitizer, *i.e.* it absorbs sunlight, which is transformed in electrical energy [11]. The advantages of organic dyes include large light absorption coefficients and easy control of the redox potentials, which are related to the positions of the highest occupied (HOMO) and of the lowest unoccupied (LUMO) molecular orbitals [12]. Numerous metal complexes and organic dyes have been synthesized and utilized as sensitizers. So far, the highest efficiency of DSSCs with metal complexes adsorbed on nanocrystalline TiO_2 reaches 13% [13].

This contribution deals with phthalocyanine (Pc) derivatives as organic pigments because of their remarkable electronic and optical properties as well as of their thermal and chemical stability. Phthalocyanines are planar 18 π-electron macro-heterocycles built from four isoindole subunits linked together through nitrogen atoms. Their extensive π-conjugated system generates intense absorption spectra, presenting two major bands: the Q band and the Soret B band. The first, usually located in the 620–700 nm wavelength region, is at the origin of the green or of the blue color of Pc's and is the strongest, with molar absorptivity (ε) values that exceed 10^5 L mol^{-1} cm^{-1}. On the other hand, the Soret band lies near 350 nm and is generally much broader and less intense. Tailoring the physical and optical properties of Pc's is achieved either by the inclusion of a metal atom into the ring or by axial and/or peripheral substitutions with a variety of ligands. Among these, dyes functionalized by electron-donating (D) and electron-accepting (A) groups to form D-π-A structures are promising owing to their broad and intense absorption spectra. Their photo-absorption is characterized by intramolecular charge transfer (ICT) excitations from the donor to the acceptor moiety of the dye, resulting in i) efficient electron injection from the acceptor into the semiconductor conduction band and ii) reduced electron-hole recombination [14]. In addition, the Pc's redox properties are suitable both for sensitization of TiO_2 films and for dye regeneration by the electrolyte. These properties make Pc's ideal candidates for incorporation in DSSCs [15–17].

In combination with experimental characterizations, quantum chemical studies on the physico-chemical properties of dye-sensitizers provide complementary information to understand the relationships between their structural, electronic, and optical properties, and their performance, and therefore to design new molecules [18–20]. In this context, the present computational chemistry investigation aims at providing better insight into the parameters that govern the intramolecular charge transfer (ICT) and photo-injection processes in Pc dyes for DSSCs. In particular, density functional theory (DFT) and time-dependent DFT (TD-DFT) calculations were performed to study the geometry, electronic

* Corresponding author.
E-mail address: benoit.champagne@unamur.be (B. Champagne).

https://doi.org/10.1016/j.optmat.2021.111315
Received 20 April 2021; Received in revised form 6 June 2021; Accepted 22 June 2021
Available online 28 July 2021

structure, and absorption spectrum of representative Pc dyes [19]. These analyses are carried out at the light of available experimental data on Zn-phthalocyanines synthesized by Cid et al. [21] and by Garcia-Iglesias et al. [22]. The structures of the Pcs' under investigation are sketched in Schemes 1 and 2. All transition metals have a formal II oxidation state.

In Scheme 1, the TT1*t*But-Zn compound possesses one substituent on each phenyl ring, three are *tert*-butyl groups and the last one is a carboxylic function. In TT2*t*But-Zn to TT5 *t*But-Zn, there is a spacer between the carboxylic group and the phenyl ring. These compounds were synthesized by Cid et al. [21] and constitute our first set of compounds. The second set of compounds in obtained by replacing the *tert*-butyls by methyls (TT1Me–Zn to TT5Me–Zn). In the third set, the Zn atom in TT1Me–Zn is replaced by other transition metals in formal oxidation state II. In the fourth set, several substituents (from 2 to 4) are carboxylic functions, the other ones being methyls. Then, in the TT6 set, there are two carboxylic functions on the same ring. When *tert*-butyls groups are on the other rings, this corresponds to the compound synthesized by Garcia-Iglesias et al. [22] (TT6*t*But-Zn). In the other TT6 derivatives, these alkyl groups are methyls while the carboxylic functions are at different positions to define various position isomers. TT7-Zn presents two carboxylic functions on each ring (Scheme 2). The next derivatives are characterized by the presence of one carboxylic function on one ring while the other rings are extended (when R = C_4H_4, this is a naphtalene ring, when it is C_8H_8, it corresponds to an anthracene). TT8 derivatives contain one naphtalene ring, TT9 derivatives have two and TT10 has three, always with Zn as transition metal atom. Finally, the TT11, TT12, and TT13 derivatives bear one (two), two (one), and three (zero) anthracene (naphtalene) units.

2. Methodological and computational details

Theoretical studies of organic pigments generally concentrate on energy gaps, the optical and the fundamental energy gaps. Both are accessible experimentally, but in different ways. The optical gap, ΔE_{opt}, corresponds to the excitation energy to the first dipole-allowed excited state. The fundamental gap, $\Delta\varepsilon_{HL} = \varepsilon_{LUMO} - \varepsilon_{HOMO} = \varepsilon_L - \varepsilon_H$, is defined by charged excitations as the difference between the first ionization potential (I) and the first electron affinity (A), $\Delta\varepsilon_{HL} = I - A$. These I and A can be determined by using photoemission and inverse photoemission, or tunneling spectroscopy involving electron removal or injection, respectively. The optical gap is often determined by measuring the onset of the absorption spectrum.

The geometries of the metallo-phthalocyanine derivatives were fully optimized at the DFT level of theory using the 6-311G(d) basis set in

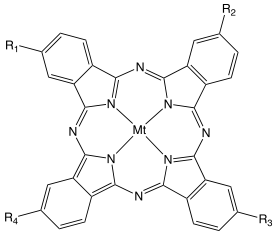

TT1-TT5

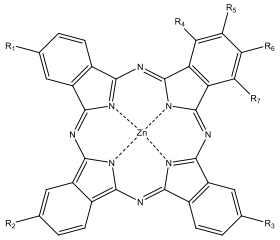

TT6

Mt	R_1	R_2	R_3	R_4	R_5	R_6	R_7	Given name
Zn	COOH	*t*-But	*t*-But	*t*-But				TT1*t*Bu-Zn[a]
Zn	O-$(CH_2)_5$-COOH	*t*-But	*t*-But	*t*-But				TT2*t*Bu-Zn[a]
Zn	Ph-COOH	*t*-But	*t*-But	*t*-But				TT3*t*Bu-Zn[a]
Zn	O-Ph-COOH	*t*-But	*t*-But	*t*-But				TT4*t*Bu-Zn[a]
Zn	Ph-CH_2=CH_2-COOH	*t*-But	*t*-But	*t*-But				TT5*t*Bu-Zn[a]
Zn	COOH	Me	Me	Me				TT1Me-Zn
Zn	O-$(CH_2)_5$-COOH	Me	Me	Me				TT2Me-Zn
Zn	Ph-COOH	Me	Me	Me				TT3Me-Zn
Zn	O-Ph-COOH	Me	Me	Me				TT4Me-Zn
Zn	Ph-CH_2=CH_2-COOH	Me	Me	Me				TT5Me-Zn
Cu	COOH	Me	Me	Me				TT1Me-Cu
Ni	COOH	Me	Me	Me				TT1Me-Ni
Co	COOH	Me	Me	Me				TT1Me-Co
Fe	COOH	Me	Me	Me				TT1Me-Fe
Mn	COOH	Me	Me	Me				TT1Me-Mn
Zn	COOH	Me	COOH	Me				TT1Me-2Ac1-Zn
Zn	COOH	COOH	Me	Me				TT1Me-2Ac2-Zn
Zn	COOH	COOH	COOH	Me				TT1Me-3Ac-Zn
Zn	COOH	COOH	COOH	COOH				TT1Me-4Ac-Zn
Zn	*t*-But	*t*-But	*t*-But	H	COOH	COOH	H	TT6*t*But-Zn[b]
Zn	Me	Me	Me	H	COOH	COOH	H	TT6Me-Zn(A)
Zn	Me	Me	Me	COOH	COOH	H	H	TT6Me-Zn(B)
Zn	Me	Me	Me	COOH	H	COOH	H	TT6Me-Zn(C)
Zn	Me	Me	Me	COOH	H	H	COOH	TT6Me-Zn(D)

Scheme 1. Structure of TT1-TT6 derivatives. See the text for more details.[a] Compounds synthesized by Cid et al. [21]; [b] Compound synthesized Garcia-Iglesias et al. [22].

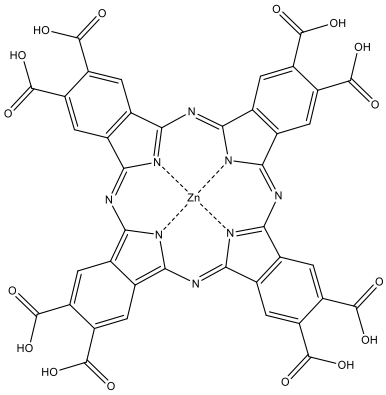

TT7

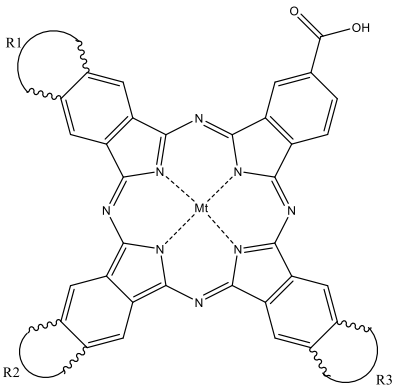

TT8-TT13

Mt	R_1	R_2	R_3	Given name
Zn		C_4H_4		TT8-1-Zn
Zn	C_4H_4			TT8-2-Zn
Zn	C_4H_4	C_4H_4		TT9-1-Zn
Zn	C_4H_4		C_4H_4	TT9-2-Zn
Zn	C_4H_4	C_4H_4	C_4H_4	TT10-Zn
Zn	C_8H_8	C_4H_4	C_4H_4	TT11-1-Zn
Zn	C_4H_4	C_8H_8	C_4H_4	TT11-2-Zn
Zn	C_8H_8	C_8H_8	C_4H_4	TT12-1-Zn
Zn	C_8H_8	C_4H_4	C_8H_8	TT12-2-Zn
Zn	C_8H_8	C_8H_8	C_8H_8	TT13-Zn
Mn	C_8H_8	C_8H_8	C_8H_8	TT13-Mn

Scheme 2. Structure of TT7-Zn (left) and of TT8-TT13 derivatives (right).

combination with a collection of exchange-correlation (xc) functionals: B3LYP [23,24], CAM-B3LYP [25], M06 [26], M06–2X [26], and ωB97X-D [27,28]. The choice of the 6-311G(d) valence triple-zeta basis set, which incorporates a set of polarization functions on the heavy atoms, has been substantiated by comparisons with the more extended cc-pVTZ basis set, as well as with less extended basis sets (Table S1). Tight convergence thresholds on the residual forces on the atoms (1.5×10^{-5} Hartree/Bohr or Hartree/radian) were applied. Subsequently, the vibrational frequencies were calculated for the ground state optimized geometries. Their real values confirm that these geometries are minima on the potential energy hypersurface.

For these ground state optimized geometries, the 30 lowest electronic excitation energies (ΔE_{0n}) and oscillator strengths (f_{0n}) were computed using the TDDFT method [29–31], again with a selection of xc functionals including global hybrids (B3LYP, M06, M06–2X) and range-separated hybrids (ωB97X-D, CAM-B3LYP) and the 6-311G(d) basis set. The optical UV/visible absorption spectra were simulated by associated each transition with a Gaussian function having a full width at half maximum (FWHM) of 0.33 eV. All UV–visible spectra in this paper have been obtained via DrawSpectrum [32].

In both the geometry optimizations and calculations of the excitation energies, different spin multiplicities were considered as a function of the nature of the transition metal: Zn (II) and Ni(II) [Singlet (S)], Cu(II) [doublet (D) and quartet (Q)], Co(II) [D, Q, and sextet (S)], Fe(II) [singlet (S), triplet (T), and quintuplet (Q)], and Mn(II) (D, Q, and S). For low-spin (*ls*) solutions of $2S+1$ spin multiplicity, spin contamination effects were corrected using the following equations [33], which provide an approximate projected correction of the unrestricted solution (APUDFT) by considering the low-spin and high-spin (*hs*) unrestricted DFT (UDFT) energies and the corresponding S^2 expectation values, which should be equal to $S(S+1)$ in absence of spin contamination.

$$E^{ls}(APUDFT) = E^{ls}(UDFT) + f_{SC}\left[E^{ls}(UDFT) - E^{hs}(UDFT)\right] \quad (1)$$

$$\text{with } f_{SC} = \frac{\langle S^2\rangle^{ls} - S(S+1)}{\langle S^2\rangle^{hs} - \langle S^2\rangle^{ls}} \quad (2)$$

For all calculations (geometry optimizations, electronic structures, excited state properties), the solvent effects were accounted for using the IEFPCM scheme [34]. This scheme approximates the solvent as a structureless polarizable continuum characterized by its macroscopic dielectric permittivity. Geometry optimizations employed the static dielectric constant (ε_0) whereas TDDFT excited state calculations used the infinite frequency value (ε_∞) since it corresponds to non-equilibrium solvation.

For push-pull systems such as metallo-phthalocyanines, CT excitations dominate the UV/vis absorption spectra and they were subjected to a detailed analysis [35]. Each transition is characterized by an excitation energy, between the ground (0) and nth excited states, ($\Delta E_{opt} = \Delta E_{0n} = E_n - E_0$), and its associated transition dipole moment:

$$\mu_{0n} = \langle 0|\hat{\mu}|n\rangle \quad (3)$$

Radiative processes are governed by the oscillator strength of the transition, which is related to the transition dipole moment:

$$f_{0n} = \frac{2}{3}\Delta E_{0n}|\mu_{0n}|^2 \quad (4)$$

The CT character of the excitations can be determined from the difference of electronic density between the ground and excited states, $\Delta\rho(\vec{r})$, following the procedure described in Ref. 35. Using this method, the distance between the barycenters of the negative and positive $\Delta\rho(\vec{r})$ defines the charge-transfer distance (d_{CT}), their integration over the whole space gives the amount of charge transferred (q_{CT}), while their product gives the CT dipole moment, $\Delta\mu_{CT} = q_{CT} \times d_{CT}$.

To further analyze the performance of organic pigments the free enthalpies of reaction were evaluated for three processes: the injection (ΔG_{inj}), the recombination (ΔG_{rec}) [11], and the regeneration (ΔG_{reg}) [36]. ΔG_{inj} describes the injection of the excited electron from the LUMO of the oxidizing pigment to the conduction band (CB) of the semiconductor:

$$\Delta G_{inj} = E_{cb} - \varepsilon_L \quad (5)$$

When the semiconductor is TiO_2, $E_{cb} = -4.0$ eV [37]. ΔG_{rec} depicts the phenomenon of return of the injected electron from the semiconductor surface to the HOMO of the pigment:

$$\Delta G_{rec} = \varepsilon_H - E_{cb} \quad (6)$$

and finally, ΔG_{reg} describes the reduction of the oxidized pigment by an electron transfer from the redox mediator to the pigment HOMO:

$$\Delta G_{reg} = \varepsilon_H - E_{redox} \quad (7)$$

A common redox couple is $3I^-/I_3^-$ having $E_{redox} = E_{I^-/I_3^-} = -4.8$ eV [37].

All the calculations were performed with the Gaussian A16 program package [38].

3. Results and discussion

3.1. Searching for a suitable XC functional for geometry optimization and electronic structure calculation

First, we searched for a reliable XC functional to predict the geometry and electronic properties (I, A, ε_H, and ε_L) of Pc's. This was done by selecting the TT1*t*But-Zn molecule (Scheme 1) where the *t*-butyl groups are replaced by methyl groups to get TT1Me–Zn. This substitution has negligible impact on the orbital energies and key structural parameters (Table S2). The geometry of TT1Me–Zn was optimized with the B3LYP, ωB97X-D, M06, and M06–2X XC functionals. We focused on the ($-\varepsilon_H$, I) and ($-\varepsilon_L$, A) quantities, which should be identical two by two in the limit of exact KS DFT [39]. The B3LYP and M06 XC functionals perform better than M06–2X and ωB97X-D (Table S3 and Figure S1). On this basis, forthcoming geometry optimizations and electronic structure calculations were carried out using the B3LYP XC functional.

3.2. Electronic properties of the TTnMe-Zn molecules (n = 1–5)

The geometries of the TTnMe-Zn (n = 1–5) molecules were optimized. These compounds present very similar HOMO-LUMO gaps (the largest difference amounts to 0.05 eV), whereas both frontier orbital energies vary by up to 0.16 eV (Table 1). Thus, the nature of the acceptor group in R_1 position has little impact to improve the performance of this series of DSSC pigments.

3.3. Effect of the nature of the transition metals on the structure and electronic properties

For a selection of transition metals, the geometries of the TT1Me-Mt compounds were fully optimized at the B3LYP/6-311G*/IEFPCM(ethanol) level (Table 2) by considering the different spin multiplicities. Besides the fact that Zn(II) and Cu(II) are naturally associated with singlet ground states, calculations predict that the ground state is a doublet (Cu and Co), a triplet

Table 1
Orbital energies (ε_L, ε_H, $\Delta\varepsilon_{HL} = \varepsilon_L - \varepsilon_H$) of TT1-TT5Me–Zn as calculated at the B3LYP/6-311G*/IEFPCM(ethanol) level.

Compound	ε_L (eV)	ε_H (eV)	$\Delta\varepsilon_{HL}$ (eV)
TT1Me–Zn	−3.13	−5.25	2.12
TT2-Me-Zn	−2.97	−5.11	2.14
TT3-Me-Zn	−3.06	−5.20	2.14
TT4-Me-Zn	−3.04	−5.21	2.17
TT5-Me-Zn	−3.06	−5.19	2.13

Table 2
Remarkable geometrical parameters of the TT1Me-Mt derivatives as obtained from geometry optimization at the B3LYP/6-311G*/IEFPCM(ethanol) level in comparison to experimental data from single-crystal X-ray diffraction. When Mt = Cu, Ni, Co, Fe and Mn, different spin multiplicities were considered. Bond lengths are given in Å while angles in degrees. For (almost) equivalent bonds and angles, averages are reported. Values in bold correspond to the ground state spin multiplicity (Table 3). Detailed geometrical parameters are given in Table S5A and S5B.

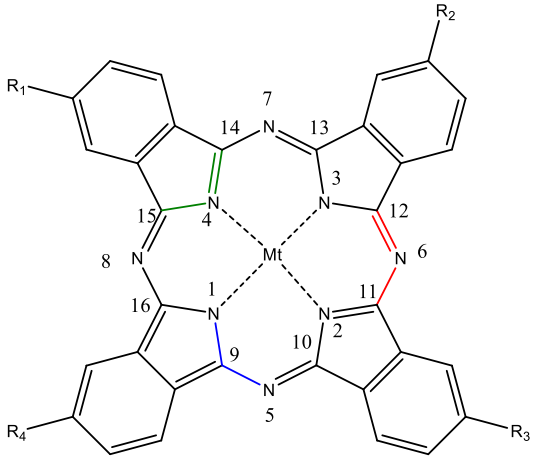

Mt [Ref]	Parameters	Experiment	Calculations	
Zn [41]	2S+1		**1**	
	Zn-N	1.972	**2.005**	
	N-Zn-N'	90.0	**90.0**	
	C-N(ring)	1.364	**1.366**	
	C-N(linker)	1.328	**1.331**	
	N(ring)-C-N(linker) (8)	127.6	**127.6**	
	C-N(linker)-C (4)	123.7	**124.9**	
	C-N(ring)-C (4)	108.9	**110.0**	
Cu [42]	2S+1		**2**	4
	Cu-N	1.952	**1.964**	1.962
	N-Cu-N'	90.0	**90.0**	89.8
	C-N(ring)	1.385	**1.370**	1.375
	C-N(linker)	1.355	**1.325**	1.329
	N(ring)-C-N(linker)	126.9	**127.6**	127.9
	C-N(linker)-C	122.3	**123.4**	122.7
	C-N(ring)-C	106.2	**108.7**	108.7
Ni [43]	2S+1		**1**	
	Ni-N	1.896	**1.917**	
	N-Ni-N'	90.0	**90.0**	
	C-N(ring)	1.379	**1.376**	
	C-N(linker)	1.302	**1.318**	
	N(ring)-C-N(linker)	126.4	**127.7**	
	C-N(linker)-C	123.1	**121.8**	
	C-N(ring)-C	106.6	**107.1**	

(*continued on next page*)

Table 2 (*continued*)

Mt [Ref]	Parameters	Experiment	Calculations		
Co [44]	2S+1		**2**	4	6
	Co-N	1.931	**1.935**	1.997	1.997
	N-Co-N'	90.0	**90.0**	90.2	90.0
	C-N(ring)	1.376	**1.374**	1.368	1.372
	C-N(linker)	1.328	**1.321**	1.330	1.333
	N(ring)-C-N(linker)	127.9	**127.6**	127.5	127.9
	C-N(linker)-C	121.4	**122.5**	124.7	123.9
	C-N(ring)-C	107.2	**107.7**	109.8	109.7
Fe [44]	2S+1		1	**3**	5
	Fe-N	1.939	1.950	**1.950**	1.941
	N-Fe-N'	90.0	90.0	**90.1**	90.0
	C-N(ring)	1.377	1.373	**1.375**	1.390
	C-N(linker)	1.331	1.323	**1.323**	1.321
	N(ring)-C-N(linker)	127.5	127.5	**127.5**	127.8
	C-N(linker)-C	122.1	123.1	**123.1**	122.3
	C-N(ring)-C	107.2	108.1	**108.1**	107.8
Mn [45]	2S+1		2	**4**	6
	Mn-N	1.954	1.961	**1.959**	1.964
	N-Mn-N'	90.0	90.0	**90.0**	90.0
	C-N(ring)	1.382	1.377	**1.385**	1.389
	C-N(linker)	1.331	1.323	**1.322**	1.326
	N(ring)-C-N(linker)	127.5	127.4	**127.4**	127.7
	C-N(linker)-C	122.8	123.7	**123.4**	123.2
	C-N(ring)-C	107.8	108.4	**108.4**	108.6

(Fe), or a quartet (Mn) (Table 3). These results are consistent with a recent work and references therein demonstrating the intermediate spin character of the ground state of Mn(II) and Fe(III) phthalocyanines (*i.e.* without substituents) [40]. For the different spin multiplicities, the optimized geometries were compared to experimental X-Ray diffraction data of similar compounds [41–45] (Table 2). When considering the spin multiplicity associated with the lowest ground state energy, the optimized bond lengths and bond angles of all compounds are in close agreement with the experimental data. Typical deviations are of the order of 1 p.m. for the distances and 1° for the angles, or less. There are a few exceptions like the Ni–N distance (difference of 0.02 p.m.) but no alternative spin multiplicity is realistic. Part of the difference might originate from solid state effects since the experimental geometries have been determined from single crystal X-ray diffraction experiments while the calculations are performed for molecules embedded in a polarizable continuum. Another source of difference comes from the experimental structures, which might be slightly different because of the presence of other substituents on the phthalocyanine core, but these variations are small. Yet, in order to highlight the impact of the TM atom, Table 2 presents data with the same core whereas the comparison with the other cores are given in SI (Table S4). In Table S4, gas electron diffraction data are also included. These allow assessing the amplitude of the surrounding effects in the crystal and confirming the ground state spin multiplicity when the differences of geometries are large enough. When considering other spin multiplicities, which correspond to higher energies, the agreement might be similar [quartet versus doublet for Cu(II), singlet versus triplet for Fe(II), and doublet or sextuplet versus quartet for Mn(II)], demonstrating that using the geometry is not sufficient to substantiate the ground state spin multiplicity. In other cases [quartet and sextet *versus* doublet for Co(II), quintuplet *versus* triplet for Fe(II)], at least for several geometrical parameters, the optimized geometries for other spin multiplicities differ from the experimental ones, demonstrating that these are not realistic ground states.

Table 3
Electronic energies relative to the lowest-energy spin multiplicity state (ΔE), S^2, ε_H, ε_L, and $\Delta\varepsilon_{HL}$ of TT1Me-Mt derivatives for different Mt atom and different spin multiplicities as calculated at the B3LYP/6-311G*/IEFPCM (ethanol) level of approximation.

Mt	2*S* + 1	$\langle S^2 \rangle$	ΔE (eV)	ε_L (eV)	ε_H (eV)	$\Delta\varepsilon_{HL}$ (eV)
Zn(II)	**1**	0		−3.13	−5.25	2.12
Cu(II)	**2**	0.753[a]	0.00	−3.19[c]	−5.30	2.11
		0.750[b]		−3.17[c]	−5.31	2.14
	4	3.769[a]	1.09	−3.11	−5.26	2.15
		3.750[b]		−3.26	−5.25	1.99
Ni(II)	**1**	0		−3.15	−5.31	2.16
Co(II)	**2**	0.755[a]	0.00	−3.08	−5.25	2.17
		0.750[b]		−3.06	−5.27	2.21
	4	3.760[a]	0.66	−3.11	−5.26	2.15
		3.750[b]		−3.27	−5.25	1.98
	6	8.773[a]	1.76	−2.93	−4.22	1.29
		8.750[b]		−4.26	−6.42	2.16
Fe(II)	1	0	1.29	−3.00	−5.21	2.21
	3	2.043[a]	0.00	−3.08	−5.26	2.18
		2.001[b]		−3.27	−5.27	2.00
	5	6.051[a]	1.16	−2.96	−4.18	1.22
		6.001[b]		−4.03	−5.11	1.08
Mn(II)	2	0.786[a]	1.69	−3.00	−5.21	2.21
		0.751[b]		−2.93	−5.28	2.35
	4	4.386[a]	0.00	−3.13	−5.19	2.06
		3.776[b]		−3.32	−4.53	1.21
	6	8.802[a]	0.38	−2.97	−4.19	1.22
		8.751[b]		−3.54	−5.13	1.59

[a] Before annihilation.
[b] After annihilation.
[c] When there are two lines, the first corresponds to α molecular orbital and the second to β molecular orbital.

For the compounds in their lowest spin state the gap ($\Delta\varepsilon_{HL}$) is little impacted by the nature of the divalent metal and it is close to 2.1–2.2 eV, (Table 3). For the triplet of TT1Me–Fe(II) it remains similar but not for the quartet of TT1Me–Mn(II) it gets as small as $\Delta\varepsilon_{HL} = 1.2$ eV. The very small variations of HOMO-LUMO gap and of their related HOMO and LUMO energies for a broad range of compounds result from the spatial distribution of the HOMO and LUMO (Figure S1–S24). Indeed, for most compounds, they are all localized on the aromatic frame, which is identical in the TT1Me-Mt series. Deviations from the 2.1–2.2 eV value of the HOMO-LUMO gap appears when the HOMO and/or the LUMO is localized on the metal atom, which occurs typically for the highest spin multiplicities [quartet and sextet of Co(II)], triplet and quintuplet of Fe(II), quartet and sextet of Mn(II)].

Though the HOMO and LUMO are localized on the aromatic rings, the LUMO extends over the carboxylic acceptor group, which is not the case of the HOMO. A difference of localization of the frontier orbitals is important for the efficiency of the electron injection step in DSSCs, where the HOMO should be localized on the donor part and LUMO on the acceptor subunit [46].

3.4. *Effect of several anchoring groups on the structure and electronic properties*

One of the phenyl groups of the Zn(II) phthalocyanine core was then substituted by two carboxylic functions, leading to different position isomers, of which the relative energy is governed by the formation of intramolecular H-bonds (Figure S25, Table 4). In comparison to the parent

Table 4
Relative total energies (Δ*E*, kJ/mol) and orbital energies (ε_L, ε_H, $\Delta\varepsilon_{HL} = \varepsilon_L - \varepsilon_H$) of TT6Me–Zn isomers as calculated at the B3LYP/6-311G*/IEFPCM(ethanol) level in comparison to the parent TT1Me–Zn compound.

Isomer	Relative energy (kJ/mol)[a]	ε_L (eV)	ε_H (eV)	$\Delta\varepsilon_{HL}$ (eV)
TT6Me–Zn-(A)	34.7	−3.30	−5.34	2.04
TT6Me–Zn-(B)	41.5	−3.33	−5.43	2.10
TT6Me–Zn-(C)	0.0	−3.33	−5.42	2.09
TT6Me–Zn-(D)	3.0	−3.40	−5.51	2.11
TT1Me–Zn	/	−3.13	−5.25	2.12
TT1Me-2Ac1-Zn	0.3	−3.26	−5.34	2.08
TT1Me-2Ac2-Zn	0.0	−3.20	−5.36	2.16
TT1Me-3Ac–Zn	/	−3.31	−5.43	2.12
TT1Me-4Ac–Zn	/	−3.36	−5.51	2.15
TT7Me–Zn	/	−3.77	−5.85	2.08

[a] The energy of TT6Me–Zn-(C) is −3942.15038 a.u. while the energy of TT1Me-2Ac1-Zn is −3902.82398 a.u.

mono-substituted Zn(II) phthalocyanine (TT1Me–Zn), this leads to a stabilization of the LUMO by about 0.2–0.3 eV while the HOMO is slightly less stabilized so that the effect on the HOMO-LUMO gap is at much a reduction by 0.1 eV. The next step was the mono-substitution of two or more phenyl rings. Again, the multiple substitutions by carboxylic groups stabilize both the HOMO and the LUMO with small impact (<0.1 eV) on the HOMO-LUMO gap (Table 4). Note that substitution on neighboring or opposite rings does not lead to significant energy difference. Then, up to two acid groups were placed on each of the four phenyl rings, leading to stabilizations of both HOMO and LUMO by as much as 0.6 eV.

Other structural modifications consists in adding fused rings (Scheme 2). Successive substitutions of the phenyl rings of the Zn(II) phthalocyanine by naphthyl and anthracenyl groups destabilize the HOMO. The typical destabilization amounts to 0.08 eV for one phenyl-to-naphtyl substitution and to 0.06 eV for one naphtyl-to-anthracenyl substitution. The impact on the LUMO is much smaller and does not exhibit any clear trend as a function of the number of fused rings. Therefore, the successive substitutions of TT1Me–Zn to form TT13Me–Zn are associated with a reduction of the gap from 2.12 eV to 1.70 eV (Table 5). Additional calculations were then carried out on the Mn derivatives of TT13-Me because we observed in Table 3 that Mn(II) is associated with small HOMO-LUMO gap. Though for the doublet, a significant decrease of $\Delta\varepsilon_{HL}$ is observed when going from TT1Me–Mn to TT13Me–Mn, the effects are reduced for the higher spin multiplicities (Table S6).

3.5. UV/visible absorption spectra and analysis of the excited states

The UV/vis absorption spectra were then simulated for the different phthalocyanine derivatives. By considering the parent compound [TT1Me–Zn(II)], one observes that the spectrum is dominated by two bands (Table S7). One band is centered around 650 nm with negligible impact of the XC functional, within the selected range, while the amount of HF exchange varies substantially from B3LYP (20%) to M06–2X (54%), and to ωB97X-D (100% at long range). The second band depends more strongly upon the XC functionals, with the smallest excitation energy (3.68 eV) with B3LYP and the largest (4.16 eV) with ωB97X-D. Note that each band is determined by several electronic transitions (for the first band, two excitations having differences of excitation energies less than 0.1 eV, and at least two for the second one). The experimental large-frequency band peaks at 680 nm [21] so that the ωB97X-D XC functional was selected for the following calculations.

For compounds TT1Me–Zn(II) to TT5Me–Zn(II) the results are presented in Table 6 and Figure S26 Variations in experimental and TDDFT λ_{max} values are small. The substituent effect is also small on the oscillator strength and the light harvesting efficiency [47].

Fig. 1 simulates the UV/visible absorption spectra of the metallo-phthalocyanines with different transition metals in their most stable spin multiplicity state while additional details are given in Table S8 and Figures S27–S31. In the case of Cu(II), Ni(II), Mn(II), the shift of the lowest-energy band is small if not negligible while for Co(II) (−22 nm) and mostly Fe(II) (−43 nm) there is a clear hypsochromic shift. These results agree with the experimental UV–vis absorption spectra, either of these compounds or of related structures having the same TM atom but different substituents [21,42,48–54]. Yet, this good agreement is generally not achieved for spin multiplicity states that are not the most stable as evidenced by difference between the doublet and quartet of Cu(II), the doublet and sextuplet of Co(II), the triplet and quintuplet of Fe(II), and the singlet/sextuplet and quadruplet of Mn(II). This further substantiates the calculated relative energies of these compounds in their different spin multiplicity states. The values of the oscillator strengh and LHE proved that all Pc's with all metals have a LHE value close to 0.95, with the exception of TT1Me–Fe(T), where it reaches only 0.59.

Table 5
Orbital energies (ε_L, ε_H, $\Delta\varepsilon_{HL} = \varepsilon_L - \varepsilon_H$) of TT8-13Me–Zn isomers as calculated at the B3LYP/6-311G*/IEFPCM(ethanol).

Compound	ε_L (eV)	ε_H (eV)	$\Delta\varepsilon_{HL}$ (eV)
TT8-1-Zn	-3.10	-5.17	2.07
TT8-2-Zn	-3.15	-5.16	2.01
TT9-1-Zn	-3.11	-5.09	1.98
TT9-2-Zn	-3.18	-5.08	1.90
TT10-Zn	-3.14	-5.01	1.87
TT11-1-Zn	-3.15	-4.94	1.79
TT11-2-Zn	-3.10	-4.95	1.85
TT12-1-Zn	-3.11	-4.89	1.78
TT12-2-Zn	-3.16	-4.87	1.71
TT13-Zn	-3.12	-4.82	1.70

Table 6
Lowest-energy dipole-allowed excited states of TT1Me-TT5Me as evaluated at the TDDFT/ωB97X-D/6-311G(d)/IEFPCM(Ethanol) level of calculation [excitation energies (ΔE_{0n}, eV), wavelength of maximum absorption of the first band ($\lambda_{max,TDDFT}$, nm, as obtained from the simulated spectra), dominant MO pairs describing the excitations, oscillator strengths, and light-harvesting efficiencies (LHE) as determined from the sum of the oscillator strengths of the two lowest energy excitations] and comparison with the experimental maximum absorption wavelengths ($\lambda_{max,exp}$, nm).

Compound	$\lambda_{max,exp}$	$\lambda_{max,TDDFT}$	MOs	ΔE_{0n}	f_{0n}	LHE
TT1Me–Zn	680	642	H-L	1.90	0.73	0.96
			H-L(+1)	1.96	0.68	
TT2Me–Zn	670	646	H-L	1.90	0.69	0.96
			H-L(+1)	1.93	0.72	
TT3Me–Zn	675	649	H-L	1.90	0.78	0.97
			H-L(+1)	1.93	0.69	
TT4Me–Zn	672	646	H-L	1.91	0.75	0.96
			H-L(+1)	1.94	0.69	
TT5Me–Zn	684	649	H-L	1.89	0.82	0.97
			H-L(+1)	1.96	0.69	

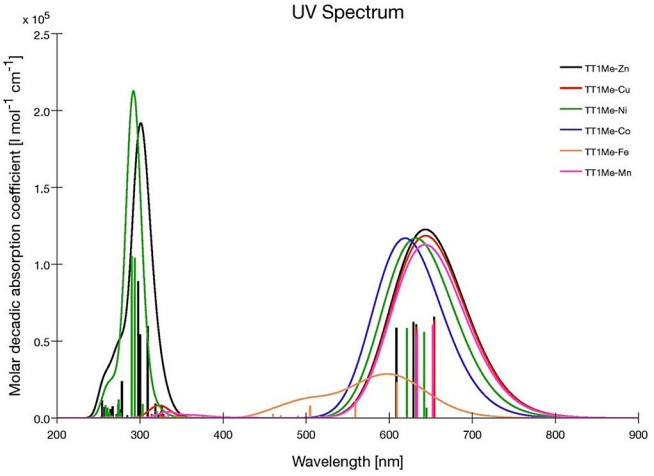

Fig. 1. UV/visible absorption spectra of the metallo-phthalocyanines as evaluated at the TDDFT/ωB97X-D/6-311G(d)/IEFPCM(Ethanol) level of calculation for their most stable spin multiplicity state.

The presence of a second anchoring group on one of the phenyl rings (isomers A-D of TT6Me–Zn) leads to a small hypsochromic shift of the first absorption band (Table S9). Differences between the isomers are negligible. The calculated maximum absorption wavelength (633 nm for the most stable isomer C) is in good agreement with experiment (684 nm) [22]. Similarly, the effect of placing a carboxylic acid function on several phenyl rings has a moderate impact (Table S10), with the exception of TT7-Zn, which presents a bathochromic shift of about 20 nm (0.1 eV). This is attributed to the presence of two COOH functions on each of the four phenyl rings. TT1Me-4Ac–Zn, which possesses four COOH functions is characterized by the largest oscillator strength, and therefore the largest LHE (0.97).

When considering compounds with one or several rings fused on the phenyl moieties, the bathochromic and hyperchromic effects are easily visible (Fig. 2, Table S11), which goes in the targeted direction of better

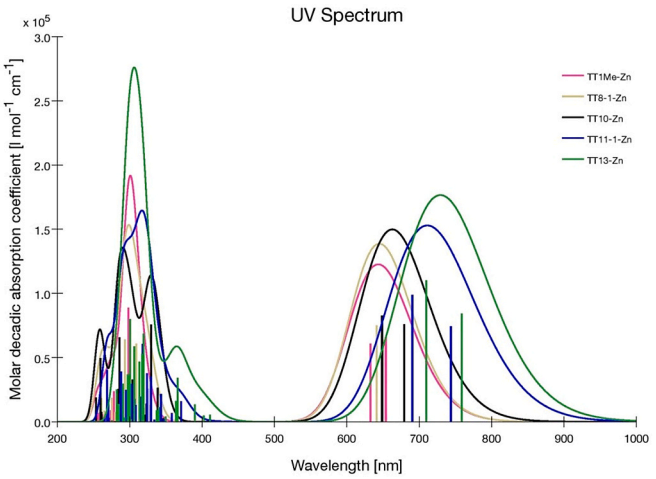

Fig. 2. UV/visible absorption spectra of the selected metallo-phthalocyanines with different number of fused rings (TT1Me–Zn, TT8-1-Zn, TT10-Zn, TT11-1-Zn, and TT3-Zn) as evaluated at the TDDFT/ωB97X-D/6-311G(d)/IEFPCM (Ethanol) level of calculation.

light harvesting pigments. Starting from the parent TT1Me–Zn compound, the maximum absorption wavelength shifts to the red by ~20 nm (or 0.05 eV) when three phenyl groups are replaced by naphtyls (TT10-Zn) and furthermore by 60 nm (0.2 eV) when these are replaced by anthracyl groups (TT13-Zn). These shifts are consistent with the experimental characterization of thin films of 2,3-naphthalocyanine that display a 0.25 eV bathochromic shift of the maximum absorption with respect to phthalocyanine [55]. At the same time, the sum of the oscillator strengths of the two low-energy transitions goes from 1.4 (TT1Me–Zn) to 1.77 (TT10-Zn), and to 2.16 (TT13-Zn). The results also highlight the relevance of the isomer (*e.g.* the difference between TT12-1-Zn and TT12-2-Zn is of the order of 20 nm). On this basis, TT13-Zn appears as an efficient light harveting compound and a promising candidate for high efficiency DSSCs. Results in Table S12 also demonstrate that replacing Zn by Mn in TT13 leads to a further bathochromic shift but it is detrimental to the oscillator strength.

3.6. Charge transfer character

Besides a large LHE value, the excited states of efficient DSSCs molecules should present large charge transfer, which can be evaluated by using the TDDFT method. Results in Table 7 demonstrate a substantial increase of μ_{CT} when large fused aromatic rings substitute the phthalocyanine core. So, from TT1Me–Zn to TT12-1-Zn, μ_{CT} is multiplied by a factor of 4. At the same time, the excitation wavelength shifts by 70 nm and the oscillator strength increases by 20%. Note that in TT13-Zn, the excitation-induced dipole moment further increases by 10% with respect to TT12-1-Zn while the oscillator strength makes a jump of 40%. The change in electron densities are drawn in Fig. 3 for representative Zn(II) Pc's.

Table 7
Charge transfer parameters of the lowest-energy dominant excitations of selected TT derivatives [q_{CT} (e), d_{CT} (Å), $\Delta\mu_{CT} = q_{CT} \times d_{CT}$ (D), within the nonequilibrium solvation approach] as calculated at the TDDFT/ωB97X-D/6-311G*/IEFPCM(Ethanol) level.

Compound	Excited state number	q_{CT}	d_{CT}	μ_{CT}
TT1Me-Zn	1	0.38	0.37	0.67
	2	0.36	0.39	0.67
TT7-Zn	1	0.40	0.01	0.01
TT8-1-Zn	1	0.43	1.73	3.57
	2	0.45	1.74	3.76
TT10-Zn	1	0.57	2.26	6.23
	2	0.42	1.59	3.22
TT11-1-Zn	1	0.47	1.62	3.67
	2	0.41	1.15	2.26
TT12-1-Zn	1	0.52	1.93	4.80
	2	0.42	1.22	2.48
TT12-2-Zn	1	0.49	1.86	4.34
	2	0.41	1.10	2.16
TT13-Zn	1	0.52	2.13	5.53
	2	0.42	1.35	2.71

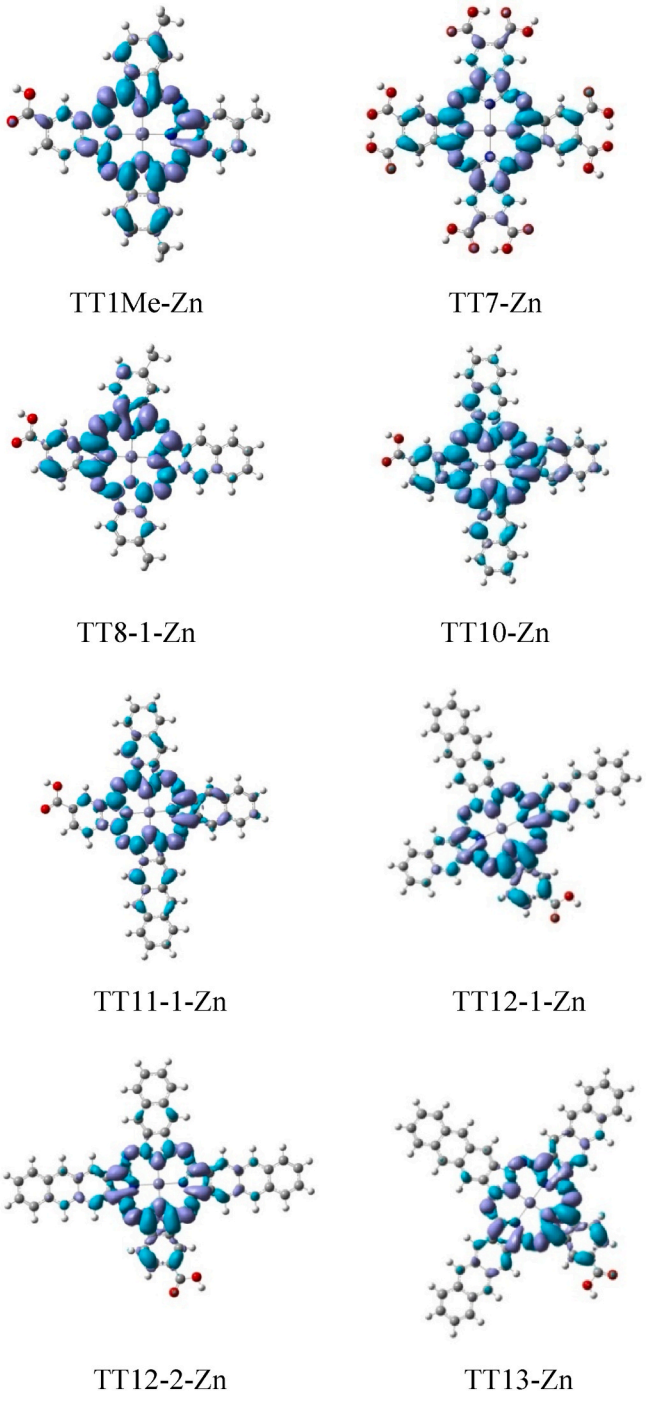

Fig. 3. Excitation-induced ωB97X-D/6-311G*/IEFPCM(Ethanol) total electron density difference [$\Delta\rho(\vec{r}) = \rho_{excited}(\vec{r}) - \rho_{ground}(\vec{r})$, isocontour value 0.0004 au] for the lowest-energy excited state of selected TT derivatives. (Purple: Positive value/Light Blue: Negative value).

3.7. Injection, recombination, and regeneration energies

To further analyze the performance of the phthalocyanines, their free energy changes of the primary processes occurring in DSSCs (electron injection, recombination, and regeneration) [11,56] were calculated. The requirements for an efficient DSSCs are i) a LUMO localized above the conduction band of the semiconductor, typically with $-\Delta G_{inj} \geq 0.5\ eV$ [57,58] since it is the driving force of the electron injection. Larger driving forces are desirable for higher V_{oc} [59] as well as for improving the short circuit current density, J_{sc} [60]. Yet, others consider that pigments possessing a lower value of $-\Delta G_{inj}$ favors the electronic injection to the CB [61]; ii) a not too large HOMO–LUMO gap ($\Delta\varepsilon_{HL} = \varepsilon_L - \varepsilon_H$) of the dye, which is closely related to its absorption band position, because more photons can be absorbed, which may lead to a larger J_{sc} and overall power conversion efficiency (η) [11,15]; iii) low values of $-\Delta G_{reg}$ to ease the regeneration of the dye [11,62]; and iv) a large $-\Delta G_{rec}$ value to avoid charge recombination and therefore to obtain a good charge separation [36]. The B3LYP/6-311G(d) data are presented in Table 8.

Most compounds present a $-\Delta G_{inj}$ larger than 0.5 eV. With the exception of TT7-Zn, the window of $-\Delta G_{inj}$ values is narrow (~0.4 eV). Multiple substitutions by carboxylic acid push the $-\Delta G_{inj}$ values closer to 0.5 eV whereas the presence of naphthyl and anthracenyl groups is detrimental since the $-\Delta G_{inj}$ values get closer to 1.0 eV. Then, concerning the $-\Delta G_{reg}$ criterion the best compounds are the TT12 and TT13 derivatives, those species with several aromatic rings. On the other hand, the largest $-\Delta G_{reg}$ values are achieved for the compounds bearing several carboxylic acid functions, with values reaching 0.5–0.7 eV.

Table 8
B3LYP/6-311G*/IEFPCM(Ethanol) $-\Delta G_{inj}$, $-\Delta G_{rec}$, and $-\Delta G_{reg}$ of phthlocyanines with different substituents and metal atoms. Only the compounds within their most stable spin multiplicity configuration were considered.

Compounds	$-\Delta G_{inj}$	$-\Delta G_{rec}$	$-\Delta G_{reg}$
TT1Me–Zn	0.87	1.25	0.45
TT2Me–Zn	1.03	1.11	0.31
TT3Me–Zn	0.94	1.20	0.40
TT4Me–Zn	0.96	1.21	0.41
TT5Me–Zn	0.94	1.19	0.39
TT1Me–Ni	0.85	1.31	0.51
TT1Me–Cu	0.81	1.30	0.50
TT1Me–Co	0.92	1.25	0.45
TT1Me–Mn	0.87	1.19	0.39
TT1Me–Fe	0.73	1.27	0.47
TT6Me–Zn (Isomer A)	0.70	1.34	0.54
TT6Me–Zn (Isomer B)	0.67	1.43	0.63
TT6Me–Zn (Isomer C)	0.67	1.42	0.62
TT6Me–Zn (Isomer D)	0.60	1.51	0.71
TT1Me-2Ac1-Zn	0.74	1.34	0.54
TT1Me-2Ac2-Zn	0.80	1.36	0.56
TT1Me-3Ac–Zn	0.69	1.43	0.63
TT1Me-4Ac–Zn	0.64	1.51	0.71
TT7-Zn	0.23	1.85	1.05
TT8-1-Zn	0.90	1.17	0.37
TT8-2-Zn	0.85	1.16	0.36
TT9-1-Zn	0.89	1.09	0.29
TT9-2-Zn	0.82	1.08	0.28
TT10-Zn	0.86	1.01	0.21
TT11-1-Zn	0.85	0.94	0.14
TT11-2-Zn	0.90	0.95	0.15
TT12-1-Zn	0.89	0.89	0.09
TT12-2-Zn	0.84	0.87	0.07
TT13-Zn	0.88	0.82	0.02
TT13-Mn	0.96	0.85	0.05

4. Conclusion

Density functional theory and time-dependent density functional theory calculations have been performed in order to investigate the electronic and optical properties of phthalocyanine derivatives, with a perspective of optimizing their performance as sensitizers in Grätzel DSSCs. The collection of phthalocyanine derivatives has been defined by starting from a well-known Zn(II) phthalocyanine and then by changing the nature of the transition metal, by adding carboxylic functions, as well as by considering extension of the aromatic rings with fused phenyl moieties. Key results encompass: i) the small impact of the transition metal (Ni, Mn, Fe, Co, and Cu *versus* Zn) on the free energies of the primary processes (injection, recombination, and regeneration), ii) the cooperative role of adding several carboxylic acid functions to optimize the injection process, and iii) the increase of the light harvesting efficiency and of the free energy of injection upon addition of fused phenyl rings. Moreover, the analysis of the molecular orbitals and the topology of the excitation-induced electron density distributions confirms the charge separation abilities of these derivatives. On the basis of these results we conjecture that compounds TT13-Zn, TT12-2-Zn, TT1Me-4Ac–Zn, and TT7-Zn are promising candidates for high efficiency DSSCs and, starting from TT1-Zn, structural modifications along these lines are worth investigating experimentally. Future work will address the electronic and optical properties of these derivatives when grafted on TiO_2 fragments [63], with a double role, i) showing the impact of the anchoring on the phthalocyanine properties and ii) studying the electron injection process.

CRediT authorship contribution statement

Mohamed Oussama Zouaghi: Supervision, Writing – original draft, conceived the project. ran the quantum chemistry calculations under the supervision. The manuscript was written. **Youssef Arfaoui:** Funding acquisition, Supervision, conceived the project. acquired the fundings for the HPC equipments, ran the quantum chemistry calculations under the supervision. **Benoît Champagne:** Supervision, Writing – original draft, conceived the project. The manuscript was written, with substantial contribution acquired the fundings for the HPC equipments. ran the quantum chemistry calculations under the supervision.

Declaration of competing interest

The authors declare that they have no known competing financial interests or personal relationships that could have appeared to influence the work reported in this paper.

Acknowledgements

The calculations were performed on the computers of the Consortium des Équipements de Calcul Intensif and particularly those of the High-Performance Computing Platform, which are supported by the FNRS-FRFC, the Walloon Region, and the University of Namur (Conventions No. GEQ U.G006.15, U.G018.19, 1610468, and RW/GEQ2016). M. O. Zouaghi thanks P. Beaujean for his help in using the CÉCI computers.

Appendix A. Supplementary data

Supplementary data to this article can be found online at https://doi.org/10.1016/j.optmat.2021.111315.

References

[1] M. Grätzel, Photoelectrochemical cells, Nature 414 (2001) 338–344.
[2] M. Grätzel, Dye-sensitized solar cells, JPPC 4 (2003) 145–153, https://doi.org/10.1016/S1389-5567(03)00026-1.
[3] M. Ye, X. Wen, M. Wang, J. Iocozzia, N. Zhang, C. Lin, Z. Lin, Recent advances in dye-sensitized solar cells: from photoanodes, sensitizers and electrolytes to counter electrodes, Mater. Today 18 (3) (2014) 155–162, https://doi.org/10.1016/j.mattod.2014.09.001.
[4] Z. Sun, M. Liang, J. Chen, Kinetics of iodine-free redox shuttles in dye-sensitized solar cells: interfacial recombination and dye regeneration, Acc. Chem. Res. 48 (6) (2015) 1541–1550, https://doi.org/10.1021/ar500337g.
[5] A. Mishra, M.K.R. Fischer, P. Bauerle, Metal-free organic dyes for dye-sensitized solar cells: from structure: property relationships to design rules, Angew. Chem. Int. Ed. 48 (2009) 2474–2499, https://doi.org/10.1002/anie.200804709.
[6] P. Selvaraj, H. Baig, T.K. Mallick, J. Siviter, A. Montecucco, W. Li, M. Paul, T. Sweet, M. Gao, A.R. Knox, S. Sundaram, Enhancing the efficiency of transparent dye-sensitized solar cells using concentrated light, Sol. Energy Mater. Sol. Cells 175 (2018) 29–34, https://doi.org/10.1016/j.solmat.2017.10.006.
[7] Y. Saygili, M. Söderberg, N. Pellet, F. Giordano, Y. Cao, A.B. Muñoz-García, S. M. Zakeeruddin, N. Vlachopoulos, M. Pavone, G. Boschloo, L. Kavan, J.E. Moser, M. Grätzel, A. Hagfeldt, M. Freitag, Copper bipyridyl redox mediators for dye-sensitized solar cells with high photovoltage, J. Am. Chem. Soc. 138 (45) (2016) 15087–15096, https://doi.org/10.1021/jacs.6b10721.
[8] X. Zhang, Y. Xu, F. Giordano, M. Schreier, N. Pellet, Y. Hu, C. Yi, N. Robertson, J. Hua, S.M. Zakeeruddin, H. Tian, M. Grätzel, Molecular engineering of potent sensitizers for very efficient light harvesting in thin-film solid-state dye-sensitized solar cells, J. Am. Chem. Soc. 138 (34) (2016) 10742–10745, https://doi.org/10.1021/jacs.6b05281.
[9] Y. Ren, D. Sun, Y. Cao, H.N. Tsao, Y. Yuan, S.M. Zakeeruddin, P. Wang, M. Grätzel, A stable blue photosensitizer for color palette of dye-sensitized solar cells reaching 12.6% efficiency, J. Am. Chem. Soc. 140 (7) (2018) 2405–2408, https://doi.org/10.1021/jacs.7b12348.
[10] J.M. Ji, H. Zhou, H.K. Kim, Rational design criteria for D–p–A structured organic and porphyrin sensitizers for highly efficient dye-sensitized solar cells, J. Mater. Chem. A. 6 (2018) 14518–14545, https://doi.org/10.1039/c8ta02281j.
[11] A. Hagfeldt, M. Grätzel, Light-induced redox reactions in nanocrystalline systems, Chem. Rev. 95 (1995) 49–68, https://doi.org/10.1021/cr00033a003.
[12] M. Grätzel, Perspectives for dye-sensitized nanocrystalline solar cells, Prog. Photovoltaics Res. Appl. 8 (2000) 171–185, https://doi.org/10.1002/(SICI)1099-159X(200001/02)8:1<171::AID-PIP300>3.0.CO;2-U.
[13] S. Mathew, A. Yella, P. Gao, R. Humphy-Baker, B.F.E. Curshod, N. Ashari-Astani, I. Tavernelli, U. Rothlisberger, M.K. Nazeeruddin, M. Grätzel, Dye-sensitized solar cells with 13% efficiency achieved through the molecular engineering of porphyrin sensitizers, Nat. Chem. 6 (2014) 242–247, https://doi.org/10.1038/nchem.1861.
[14] A. Hagfeldt, G. Boschloo, L. Sun, L. Kloo, H. Petterson, Dye-sensitized solar cells, Chem. Rev. 110 (2010) 6595–6663, https://doi.org/10.1021/cr900356p.
[15] L. Yang, L. Guo, Q. Chen, H. Sun, J. Liu, X. Zhang, X. Pan, S. Dai, Theoretical design and screening of panchromatic phthalocyanine sensitizers derived from TT1 for dye-sensitized solar cells, J. Mol. Graph. Model. 34 (2012) 1–9, https://doi.org/10.1016/j.jmgm.2011.12.001.
[16] M. Ince, J.H. Yum, Y. Kim, S. Mathew, M. Grätzel, T. Torres, M.K. Nazeeruddin, Molecular engineering of phthalocyanine sensitizers for dye sensitized solar cells, J. Phys. Chem. C 118 (30) (2014) 17166–171170, https://doi.org/10.1021/jp502447y.
[17] M.E. Ragoussi, M. Ince, T. Torres, Recent advances in phthalocyanine-based sensitizers for dye-sensitized solar cells, Eur. J. Org Chem. (2013) 6475–6489, https://doi.org/10.1002/ejoc.201301009.
[18] M. Pastore, E. Mosconi, F. De Angelis, M. Grätzel, A computational investigation of organic dyes for dye-sensitized solar cells: benchmark, strategies, and open issues, J. Phys. Chem. C 114 (2010) 7205–7212, https://doi.org/10.1021/jp100713r.
[19] A. Vlcek, S. Zalis, Modeling of charge-transfer transitions and excited states in d6 transition metal complexes by DFT techniques, Coord. Chem. Rev. 251 (2007) 258–287, https://doi.org/10.1016/j.ccr.2006.05.021.
[20] Q. Zhou, Z.F. Liu, T.J. Marks, P. Darancet, Electronic structure of metallophthalocyanines, MPc (M = Fe, Co, Ni, Cu, Zn, Mg) and fluorinated MPc, J. Phys. Chem. 125 (2021) 4055–4061, https://doi.org/10.1021/acs.jpca.0c10766.
[21] J.J. Cid, M. Garcia-Iglesias, J.H. Yum, A. Forneli, J. Albero, E. Martinez-Ferrero, P. Vazquez, M. Grätzel, M.K. Nazeeruddin, E. Palomares, T. Torres, Structure–function relationships in unsymmetrical zinc phthalocyanines for dye-sensitized solar cells, Chem. Eur J. 15 (2009) 5130–5137, https://doi.org/10.1002/chem.200801778.
[22] M. Garcia-Iglesias, J.H. Yum, R. Humphry-Backer, S.M. Zakeerudin, P. Péchy, P. Vazquez, E. Palomares, T. Torres, Effect of anchoring groups in zinc phthalocyanine on the dye-sensitized solar cell performance and stability, Chem. Sci. 2 (2011) 1145–1150, https://doi.org/10.1039/c0sc00602e.
[23] A.D. Becke, Density-functional thermochemistry. III. The role of exact exchange, J. Chem. Phys. 98 (1993) 5648, https://doi.org/10.1063/1.464913.
[24] P.J. Stephens, J.F. Devlin, C.F. Chabalowski, M.J. Frisch, Ab initio calculation of vibrational absorption and circular dichroism spectra using density functional force fields, J. Chem. Phys. 98 (45) (1994) 11623–11627, https://doi.org/10.1021/j100096a001.
[25] T. Yanai, D.P. Tew, N.C. Handy, A new hybrid exchange–correlation functional using the Coulomb-attenuating method (CAM-B3LYP), Chem. Phys. Lett. 393 (2004) 51–57, https://doi.org/10.1016/j.cplett.2004.06.011.
[26] Y. Zhao, D.G. Truhlar, The M06 suite of density functionals for main group thermochemistry, thermochemical kinetics, noncovalent interactions, excited states, and transition elements: two new functionals and systematic testing of four M06-class functionals and 12 other functionals, Theor. Chem. Acc. 120 (2008) 215–241, https://doi.org/10.1007/s00214-007-0310-x.
[27] J. Chai, M. Head-Gordon, Long-range corrected hybrid density functionals with damped atom–atom dispersion corrections, Phys. Chem. Chem. Phys. 10 (2008) 6615–6620, https://doi.org/10.1039/B810189B.
[28] J.D. Chai, M. Head-Gordon, Systematic optimization of long-range corrected hybrid density functional, J. Chem. Phys. 128 (2008), 084106, https://doi.org/10.1063/1.2834918.
[29] M.E. Casida, in: D.P. Chong (Ed.), Recent Advances in Density Functional Methods, vol. 1, World Scientific, Singapore, 1995.
[30] R. Bauernschmitt, R. Ahlrichs, Calculation of excitation energies within time-dependent density functional theory using auxiliary basis set expansions, Chem. Phys. Lett. 256 (1996) 454–464, https://doi.org/10.1016/0009-2614(96)00440-X.
[31] D.J. Tozer, N.C. Handy, J. Chem. Phys. 109 (1998) 10180–10189, https://doi.org/10.1063/1.477711.
[32] V. Liégeois, DrawSpectrum, UNamur. https://www.unamur.be/drawspectrum.
[33] M. Nakano, R. Kishi, T. Nitta, T. Kubo, K. Nakasuji, K. Kamada, K. Ohta, B. Champagne, E. Botek, K. Yamaguchi, Second hyperpolarizability (γ) of singlet diradical system: dependence of γ on the diradical character, J. Phys. Chem. 109 (2005) 885–891, https://doi.org/10.1021/jp046322x.
[34] J. Tomasi, B. Mennucci, R. Cammi, Quantum mechanical continuum solvation models, Chem. Rev. 105 (2005) 2999–3093, https://doi.org/10.1021/cr9904009.
[35] T. Le Bahers, C. Adamo, I. Ciofini, A qualitative index of spatial extent in charge-transfer excitations, J. Chem. Theor. Comput. 7 (2011) 2498–2506, https://doi.org/10.1021/ct200308m.
[36] S.A. Haque, E. Palomares, B.M. Cho, A.M.M. Green, N. Hirata, D.R. Klug, J. R. Durrant, Charge separation versus recombination in dye-sensitized nanocrystalline solar cells: the minimization of kinetic redundancy, J. Am. Chem. Soc. 127 (2005) 3456–3462, https://doi.org/10.1021/ja0460357.
[37] J.L. Luo, Q.S. Li, L.N. Yang, Z.Z. Sun, Z.S. Li, Theoretical design of porphyrazine derivatives as promising sensitizers for dye-sensitized solar cells, RSC Adv. 4 (2014) 20200–20207, https://doi.org/10.1039/c4ra02204a.
[38] Gaussian 16, Revision B.01 M.J. Frisch, G.W. Trucks, H.B. Schlegel, G.E. Scuseria, M.A. Robb, J.R. Cheeseman, G. Scalmani, V. Barone, G.A. Petersson, H. Nakatsuji, X. Li, M. Caricato, A.V. Marenich, J. Bloino, B.G. Janesko, R. Gomperts, B. Mennucci, H.P. Hratchian, J.V. Ortiz, A.F. Izmaylov, J.L. Sonnenberg, D. Williams-Young, F. Ding, F. Lipparini, F. Egidi, J. Goings, B. Peng, A. Petrone, T. Henderson, D. Ranasinghe, V.G. Zakrzewski, J. Gao, N. Rega, G. Zheng, W. Liang, M. Hada, M. Ehara, K. Toyota, R. Fukuda, J. Hasegawa, M. Ishida, T. Nakajima, Y. Honda, O. Kitao, H. Nakai, T. Vreven, K. Throssell, J. A. Montgomery Jr., J.E. Peralta, F. Ogliaro, M.J. Bearpark, J.J. Heyd, E. N. Brothers, K.N. Kudin, V.N. Staroverov, T.A. Keith, R. Kobayashi, J. Normand, K. Raghavachari, A.P. Rendell, J.C. Burant, S.S. Iyengar, J. Tomasi, M. Cossi, J. M. Millam, M. Klene, C. Adamo, R. Cammi, J.W. Ochterski, R.L. Martin, K. Morokuma, O. Farkas, J.B. Foresman, D.J. Fox, Gaussian, Inc., Wallingford CT, 2016.
[39] L. Kronik, T. Stein, S. Rafaely-Abramson, R. Baer, Excitation gaps of finite-sized systems from optimally tuned range-separated hybrid functionals, J. Chem. Theor. Comput. 8 (2012) 1515–1531, https://doi.org/10.1021/ct2009363.
[40] S. Carlotto, M. Sambi, F. Sedona, A. Vittadini, M. Casarin, A theoretical study of the occupied and unoccupied electronic structure of high- and intermediate-spin transition metal phthalocyaninato (Pc) complexes: VPc, CrPc, MnPc, and FePc, Nanomaterials 11 (1) (2021) 54, https://doi.org/10.3390/nano11010054.
[41] D. Li, S. Ge, T. Yuan, J. Gong, B. Huang, W. Tie, W. He, Green synthesis and characterization of crystalline zinc phthalocyanine and cobalt phthalocyanine prisms by a simple solvothermal route, CrystEngComm 20 (2018) 2749–2758, https://doi.org/10.1039/C8CE00215K.
[42] A. Hoshino, Y. Takenaka, H. Miyaji, Redetermination of the crystal structure of α-copper phthalocyanine grown on KCl, Acta Crystallogr. B59 (2003) 393–403, https://doi.org/10.1107/S010876810300942X.
[43] M. Helliwell, S.J. Teat, S.J. Coles, W. Reeve, Temperature-resolved study of the structural behaviour of nickel octahexyl phthalocyanine up to the liquid crystal transition, Acta Crystallogr. B59 (2003) 617–624, https://doi.org/10.1107/S0108768103014708.
[44] J. Janczak, R. Kubiak, Stereochemistry and properties of the M(II) - N(py) coordination bond in the low-spin dipyridinated iron(II) and cobalt(II) phthalocyanines, Inorg. Chim. Acta. 342 (2003) 64–76, https://doi.org/10.1016/S0020-1693(02)01060-5.
[45] J. Janczak, R. Kubiak, M. Sledz, H. Borrmann, Y. Grin, Synthesis, structural investigations and magnetic properties of dipyridinated manganese phthalocyanine, MnPc(py)2, Polyhedron 22 (2003) 2689–2697, https://doi.org/10.1016/S0277-5387(03)00361-9.
[46] M.P. Balanay, D.H. Kim, DFT/TD-DFT molecular design of porphyrin analogues for use in dye-sensitized solar cells, Phys. Chem. Chem. Phys. 10 (2008) 5121–5127, https://doi.org/10.1039/b806097e.
[47] R. Meenakshi, Spectral investigations, inhibition efficiency analysis and a TD-DFT study on tuning the light harvesting efficiency (LHE) of heterocyclic 5-nitro-1,3-benzodioxole as a photosensitizer for dye sensitized solar cells (DSSCs), RCS Adv 6 (2016) 63690–63703, https://doi.org/10.1039/C6RA07550A.
[48] J. Obirai, T. Nyokong, Synthesis, spectral and electrochemical characterization of mercaptopyrimidine-substituted cobalt, manganese and Zn (II) phthalocyanine complexes, Electrochim. Acta 50 (2005) 3296–3304, https://doi.org/10.1016/j.electacta.2004.12.003.

[49] M.M. El-Nahass, K.F. Abd-El-Rahman, A.A.A. Darwish, Fourier-transform infrared and UV–vis spectroscopes of nickel phthalocyanine thin films, Mater. Chem. Phys. 92 (2005) 185–189, https://doi.org/10.1016/j.matchemphys.2005.01.008.
[50] X. Zhou, J. Li, X. Wang, K. Jin, W. Ma, Oxidative desulfurization of dibenzothiophene based on molecular oxygen and iron phthalocyanine, Fuel Process. Technol. 90 (2009) 317–323, https://doi.org/10.1016/j.fuproc.2008.09.002.
[51] B.O. Agboola, I.K. Ozoemena, T. Nyokong, Electrochemical properties of benzylmercapto and dodecylmercapto tetra substituted nickel phthalocyanine complexes: electrocatalytic oxidation of nitrite, Electrochim. Acta 51 (2006) 6470–6478, https://doi.org/10.1016/j.electacta.2006.04.033.
[52] M. Yoneyama, M. Sugi, M. Saito, K. Ikegami, S. Kuroda, S. Iizima, Photoelectric properties of copper phthalocyanine Langmuir-blodgett film, Jpn. J. Appl. Phys. 25 (1986) 961–965, https://doi.org/10.1143/JJAP.25.961.
[53] G. Syfri, Q. Chen, Y. Lin, Y. Wang, E. Nouri, Z. Xu, P. Lianos, Soluble butyl substituted copper phthalocyanine as alternative hole-transporting material for solution processed perovskite solar cells, Electrochim. Acta 212 (2016) 929–933, https://doi.org/10.1016/j.electacta.2016.07.047.
[54] R. Baker, D.P. Wilikinson, J. Zhang, Facile synthesis, spectroscopy and electrochemical activity of two substituted iron phthalocyanines as oxygen reduction catalysts in an acidic environment, Electrochim. Acta 54 (2009) 3098–3102, https://doi.org/10.1016/j.electacta.2008.12.003.
[55] A. Hirao, T. Akiyama, T. Okujima, H. Yamada, H. Uno, Y. Sakai, S. Aramaki, N. Ono, Soluble precursors of 2,3-naphthalocyanine and phthalocyanine for use in thin film transistors, Chem. Commun. (2008) 4714–4716, https://doi.org/10.1039/B811674A.
[56] S. Daoudi, A. Semmeq, M. Badawi, X. Assfeld, Y. Arfaoui, M. Pastore, Electronic structure and optical properties of isolated and TiO2-grafted free base porphyrins for water oxidation: a challenging test case for DFT and TD-DFT, J. Comput. Chem. 40 (29) (2019) 2530–2538, https://doi.org/10.1002/jcc.26027.
[57] S.M. Pratik, A. Datta, Computational design of concomitant type-I and type-II porphyrin sensitized solar cells, Phys. Chem. Chem. Phys. 15 (2013) 18471–18481, https://doi.org/10.1039/c3cp53193g.
[58] T. Gomez, F. Jaramillo, E. Schott, R. Arratia-Pérez, X. Zarate, Simulation of natural dyes adsorbed on TiO2 for photovoltaic applications, Sol. Energy 142 (2017) 215–223, https://doi.org/10.1016/j.solener.2016.12.023.
[59] J. Xu, L. Zhu, L. Wang, L. Liu, Z. Bai, L. Wang, W. Xu, The effect of anchoring group number on molecular structures and absorption spectra of triphenylamine sensitizers: a computational study, J. Mol. Model. 18 (2012) 1767–1777, https://doi.org/10.1007/s00894-011-1208-z.
[60] L.H. Han, C.R. Zhang, J.W. Zhe, N.Z. Jin, Y.L. Shen, W. Wang, J.J. Gong, Y.H. Chen, Z.J. Liu, Understanding the electronic structures and absorption properties of porphyrin sensitizers YD2 and YD2-o-C8 for dye-sensitized solar cells, Int. J. Mol. Sci. 14 (2013) 20171–20188, https://doi.org/10.3390/ijms141020171.
[61] R. Milan, G.S. Selopal, M. Cavazzini, S. Orlandi, R. Boaretto, S. Caramori, I. Concina, G. Pozzi, Dye-sensitized solar cells based on a push-pull zinc phthalocyanine bearing diphenylamine donor groups: computational predictions face experimental reality, Sci. Rep. 7 (2018) 15675, https://doi.org/10.1038/s41598-017-15745-3.
[62] T. Daeneke, A.J. Mozer, Y. Uemura, S. Makuta, M. Fekete, Y. Tachibana, N. Koumura, U. Bach, L. Spiccia, Dye regeneration kinetics in dye-sensitized solar cells, J. Am. Soc. 134 (2012) 16925–16928, https://doi.org/10.1021/ja3054578.
[63] Y. Bai, I. Mora-Sero, F. De Angelis, J. Bisquert, P. Wang, Titanium dioxide nanomaterials for photovoltaic applications, Chem. Rev. 114 (2014) 10095–10130, https://doi.org/10.1021/cr400606n.